High-Power Microwave Generation from Large-Orbit Devices

W. W. DESTLER, MEMBER, IEEE, E. CHOJNACKI, R. F. HOEBERLING, W. LAWSON, MEMBER, IEEE,
A. SINGH, FELLOW, IEEE, AND C. D. STRIFFLER, MEMBER, IEEE

Invited Review Paper

Abstract—Experimental and theoretical studies at the University of Maryland on the production of high-power microwave radiation in cusp-injected, large-orbit devices are reviewed. Three classes of devices belonging to this category are discussed. In the first case, an axis-encircling rotating electron beam interacts via the negative mass instability with the modes of a smooth cylindrical waveguide, producing broad-band radiation at multiple harmonics of the electron cyclotron frequency. In the second case, the beam interacts with a multiresonator magnetron circuit designed to provide mode control, resulting in high-power radiation at a desired cyclotron harmonic. In the third case, the beam interacts with a transverse wiggler magnetic field produced by samarium–cobalt magnets placed interior and/or exterior to the beam. In this case the interaction is analogous to a circular geometry free-electron laser. The most recent experimental results from all three configurations are reviewed and compared with theoretical expectations. The possibility of enhanced operational efficiency in all of these devices by electron energy recovery is discussed, and a design for a first experiment to test this concept is presented.

I. INTRODUCTION

MICROWAVE RADIATION from axis-encircling rotating electron beams or E-layers was first observed in early studies of the electron ring accelerator concept in laboratories at Berkeley, Dubna (Soviet Union), Garching (West Germany), Karlsruhe (West Germany), and the University of Maryland [1]–[4]. In these experiments, where the goal was the production of dense electron rings or E-layers with self-electric fields sufficiently large to allow for ion trapping and acceleration, a substantial loss in average beam radius was observed over a time scale of 2–100 gyroperiods. This reduction in radius was attributed to electron energy loss due to coherent synchrotron radiation produced by an azimuthal bunching of the beam electrons. This azimuthal bunching was attributed to the negative mass instability.

The first experimental investigation of the possible exploitation of this radiative mechanism to efficiently produce microwaves was reported by Jory [5], who investigated azimuthal bunching of large-orbit rotating electron

beams due to negative mass effects and associated cavity excitation at frequencies in the range 48–96 GHz. The first pulse line experiment of this type was reported by Granatstein *et al.* [6]. In these experiments, a rotating beam was produced by passing a hollow nonrotating beam through a narrow magnetic cusp. Observed microwave power was about 1 percent of the injected beam power and radiation was observed at various harmonics of the electron cyclotron frequency. Sprangle [7] reported a related theoretical analysis based on a resonant interaction of beam cyclotron modes with the TE or TM waveguide modes of the downstream drift chamber. Uhm and Davidson have also reported related theoretical studies of the negative mass instability in rotating electron beams [8].

At the University of Maryland, interest in axis-encircling rotating electron beams as high-power microwave sources developed as an outgrowth of the Maryland Electron Ring Accelerator project, where ring quality was observed to be severely degraded by electron energy losses due to microwave radiation. A program to investigate such configurations as high-power microwave sources was initiated in 1977, and related experimental and theoretical work has continued to the present time [9]–[16]. This work has been complemented by theoretical and experimental studies undertaken at numerous other laboratories [17]–[23].

To date, we have investigated radiation production from rotating electron beams in three different experimental configurations. In the first, the rotating beam interacts resonantly with the modes of a smooth cylindrical conducting boundary, and broad-band radiation is produced by the interaction of beam cyclotron modes with the TE and TM modes of the cylindrical waveguide. In the second, the beam interacts with a multiresonator magnetron circuit, which provides mode control and allows for operation at a specified cyclotron harmonic. We refer to both of these configurations as large-orbit gyrotrons. In the third, the beam interacts with a transverse wiggler magnetic field produced by samarium–cobalt magnets located interior and/or exterior to the beam. This configuration is basically a circulating free-electron laser.

In this paper, the major experimental configurations that have been studied under this program at the University of Maryland are reviewed and compared with the results of

related theory. New results from an experiment constructed at Los Alamos National Laboratory to investigate microwave radiation in such devices at low harmonic number are also described, as are the first results from a program that is currently being initiated to investigate the possibility of increasing overall device efficiency by recovering a significant fraction of the energy in the spent electrons.

A discussion of the formation of high-quality rotating electron beams by cusp injection is contained in Section II of this paper. Large-orbit gyrotrons are described both theoretically and experimentally in Section III, and the circulating free-electron laser experiments are described in Section IV. A discussion of electron energy recovery in such devices is contained in Section V, and conclusions are drawn in Section VI.

II. CUSP-INJECTED BEAMS

The rotating beams used in the large-orbit experiments were generated by passing annular, linearly streaming beams through nonadiabatic magnetic transitions (magnetic cusps). This technique has proven to be an efficient way to generate high-current beams with large perpendicular energies. Studies performed to further both the theoretical and the experimental understanding of cusp-injected beams are reviewed in this section.

A. Theoretical Discussion [24]-[27]

1. Analytic Modeling: The axial field for an ideal magnetic cusp is depicted in Fig. 1(a) and is given by

$$\vec{B}(r, z) = \begin{cases} -B_1\hat{z}, & z < 0 \\ +B_2\hat{z}, & z > 0. \end{cases} \quad (1)$$

Such a field could be generated by two semi-infinite solenoids extending to $\pm\infty$ in the $\hat{z}$ direction which are separated by an infinitesimally thin iron plate with $\mu_r = \infty$ in the $z = 0$ plane.

An ideal diode is located upstream (in the half-plane defined by $z < 0$) and accelerates all electrons to the same velocity $\vec{v} = v_0\hat{z}$ (see Fig. 2(a)). The cathode emitter strip has an average radius r_0 and a radial width Δr. An electron emitted at a radius r (where $|r - r_0| < \Delta r/2$) passes through a slit in the anode and continues through the cusp. Downstream (in the half-space $z > 0$), the electron executes a helical orbit characterized by a Larmor radius $r_L = r[1 + (B_1/B_2)]/2$; a guiding center radius $r_g = r[1 - (B_1/B_2)]$; a perpendicular velocity $v_\perp = r_L\Omega_0$, where $\Omega_0 = eB_2/(m_0\gamma_0)$ and $\gamma_0 = [1 - (v_0/c)^2]^{-1/2}$; and a parallel velocity $v_z = (v_0^2 - v_\perp^2)^{1/2}$.

Several conclusions follow immediately from the ideal model. First, for any beam with finite thickness, the cusp introduces a velocity shear in the beam (with $\Delta v_\perp/v_{\perp 0} = \Delta r/r_0$). Second, there is an energy cutoff defined by $v_0 = v_\perp$, below which particles are reflected by the cusp. Finally, the electrons encircle the axis (large-orbit oper-
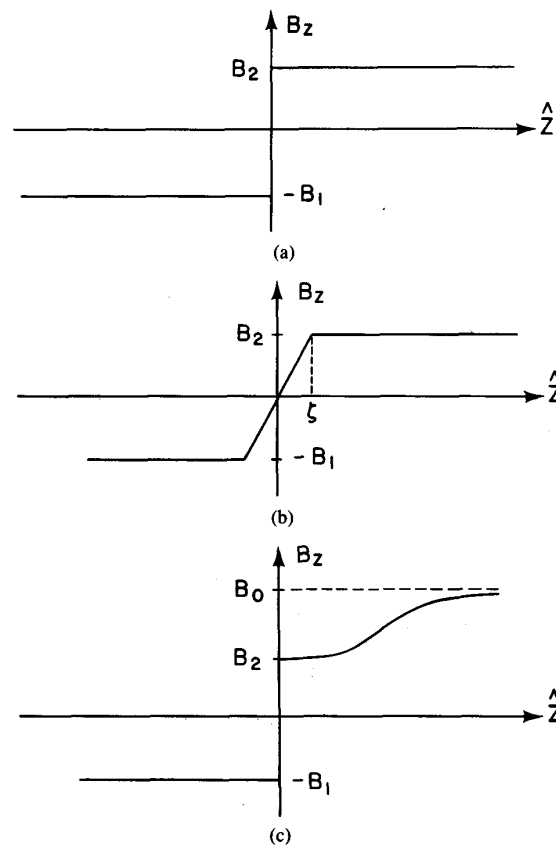

Fig. 1. Axial field profiles: (a) ideal cusp, (b) linear cusp, and (c) magnetic compression after cusp.
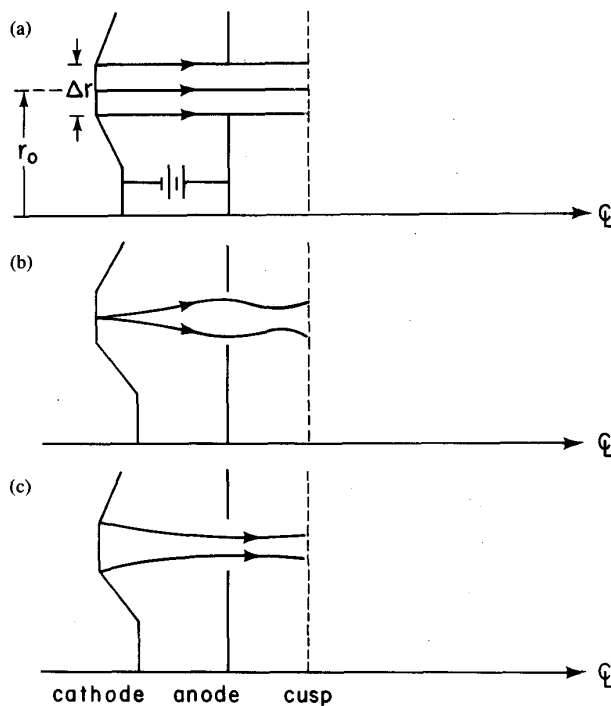

Fig. 2. Diode configuration: (a) ideal case, (b) incoherent off-centering, and (c) beam thickness reduction.

ation) if and only if $B_1/B_2 > 0$; i.e., a field reversal must occur.

A special case of interest is balanced cusp operation, where $B_1 = B_2$. For this case, $r_g = 0$, which means that all electrons have their guiding centers on the axis and the beam thickness remains Δr. In gyrotron operation, $r_g = 0$ facilitates high harmonic operation because an *m*th harmonic beam density perturbation interacts only with TE_{mn} waveguide modes at grazing intersections (see Section III-A).

Incoherent off-centering occurs when we assume that the cusp is ideal but that electrons obtain finite perpendicular energy in the diode (Fig. 2(b)). If we denote the upstream and downstream Larmor and guiding center radii r_{Lu}, r_{gu}, r_{Ld}, and r_{gd}, respectively, then for balanced cusps, $r_{gd} = r_{Lu}$ and $r_{Ld} = r_{gu}$. This result also implies that a second cusp can be used to convert a rotating beam to a linear beam for energy recovery, as will be discussed in Section V.

Coherent off-centering, on the other hand, occurs when the cusp has a finite transition length from $-B_1$ to B_2 and the diode is ideal (Fig. 1(b)). Assuming a piecewise (balanced) linear model for B_z with a full-width transition length of 2ζ, an approximate expression for the guiding center is

$$\Delta r_g = \zeta \left[2\eta - (\eta^2 - 1)^{1/2} - \eta^2 \sin^{-1} \left(\frac{1}{\eta} \right) \right] \quad (2)$$

where $\eta = v_0/(r_0 \Omega_0)$. For a thin beam, this off-centering results in an oscillatory beam envelope, with a wavelength given by

$$\lambda = 2\pi r_0 (\eta^2 - 1)^{1/2}. \quad (3)$$

Efficient large-orbit microwave production requires a low velocity spread, which in turn limits the relative beam thickness. For a given cathode emitter radius Δr, beam current is limited by the maximum cathode loading possible. This may depend on cathode material, peak electric field capability, emission process, etc. Two possible methods for increasing beam power have been considered. The first method involves the use of focus electrodes to uniformly compress the beam thickness in the diode while maintaining the average beam radius (Fig. 2(c)). If the final thickness is $|c_t| \Delta r$, then for thin beams,

$$\frac{\Delta v_\perp}{v_{\perp 0}} = \frac{\Delta r}{r_0} \frac{(1 - f_d) c_t + 2f_d}{1 + f_d} \quad (4)$$

where $f_d = B_1/B_2$. There are two important conclusions. First, a balanced cusp has $f_d = 1$, and there is no reduction in velocity spread. Second, if $c_t = -2f_d/(1 - f_d)$, then $\Delta v_\perp = 0$ after an ideal cusp, and large emitter strips could be used. The second method involves adding an adiabatic compression region after the cusp to increase the field from $+B_2$ to the microwave circuit value of B_0, as in Fig. 1(c) ($B_0 = B_2$ in the preceding discussion). For $B_0/B_2 = f_m$, the average cathode radius satisfies $r_0 \propto$

$f_m^{1/2}$ and current capability increases linearly with f_m. This enhancement is limited by the ability to create a suitable compression field profile.

2. Numeric Modeling: For tenuous beams, self-fields can be neglected in the transition region when it is sufficiently narrow. Thus, single particle techniques can be used to numerically integrate electrons through general magnetic cusps. Profiles are assumed for $B_r(r_0, z)$ and $B_z(r_0, z)$, and the magnetic field elsewhere is found using an expansion about r_0 that guarantees a zero divergence of B for all truncated series. This method is convenient for experimental purposes: The B_r and B_z field profiles can be measured at the average beam radius and fit to analytic models by least squares techniques so that particle simulations can be compared to beam envelope measurements.

For design purposes, analytic forms for $B_r(r_0, z)$ and $B_z(r_0, z)$ can be assumed and used to examine particle motion in finite transitions. For narrow transitions, a piecewise-linear model is used:

$$B_z(r_0, z)$$

$$= \begin{cases} \dfrac{1}{2} \left[(B_2 - B_1) + (B_2 + B_1) \dfrac{z}{\zeta} \right], & |z| \leq \zeta \\[2ex] \dfrac{1}{2} \left[(B_2 - B_1) + (B_2 + B_1) \dfrac{z}{|z|} \right], & |z| > \zeta \end{cases}$$

$$(5a)$$

and

$$B_r(r_0, z) = \begin{cases} -\dfrac{r_0}{4\zeta} (B_2 + B_1), & |z| \leq \zeta \\[2ex] 0, & |z| > \zeta. \end{cases} \quad (5b)$$

For longer transitions a smooth model is used:

$$B_z(r_0, z) = \frac{1}{2} \left[(B_2 - B_1) + (B_2 + B_1) \tanh (z/\zeta) \right]$$

$$(6a)$$

and

$$B_r(r_0, z) = -\frac{r_0}{4\zeta} (B_2 + B_1) \exp \left[-\frac{\pi}{4} \left(\frac{z}{\zeta} \right)^2 \right]. \quad (6b)$$

In Fig. 3, the guiding center radius due to coherent off-centering is plotted as a function of transition width ζ. The solid line indicates the analytic prediction from (2), the circles indicate the piecewise-linear simulation results (5), and the squares indicate the hyperbolic tangent simulation results (6), with an effective transition length found by a least squares fit of the two models. All estimates agree well. The parameters are taken from the hot cathode experiment (see Section III).

Modeling of electron guns and adiabatic compression regions must be done with electron trajectory codes that include self-fields, since they usually cannot be neglected. For this purpose, a square mesh code developed
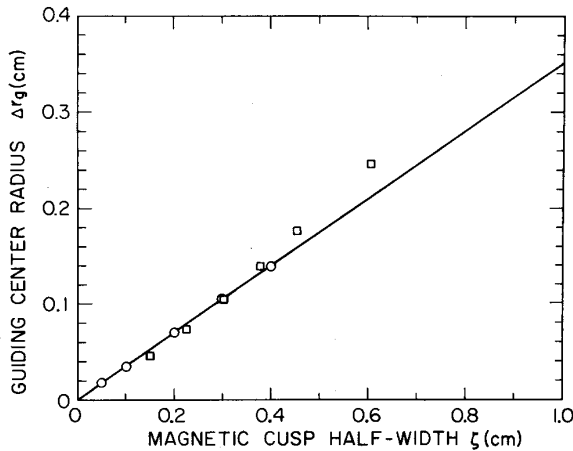
Fig. 3. Coherent off-centered guiding center radius as a function of cusp width. The line represents the analytic model, the circles indicate the piecewise-linear numeric model, and the squares indicate the hyperbolic tangent numeric model.

by W. B. Herrmannsfeldt [28] is used. Simulations of the compression region indicate that it is straightforward to design field profiles to compress beams from both balanced and unbalanced cusps. For $r_g = 0$ beams, velocity spread remains essentially unchanged in the compression region. However, intense $r_g \neq 0$ beams can undergo drastic changes in velocity spread during compression. With proper adjustment of beam thickness in the diode, it has been shown that these self-field effects can be used to further reduce velocity spread.

B. Experimental Discussion [16], [24], [25], [29], [30]

1. Cold Cathode Experiments: There are two field-reversal devices in operation at the University of Maryland. The cold cathode device generates 1–2-MV, 4–10-kA, 35-ns pulses via a Marx generator/Blumlein system. The beam is generated by field emission from a graphite knife-edged cathode having a radius of 6 cm. The field is generated by two sets of pancake coils separated by an iron plate (see Fig. 4) and has a transition length of $\zeta = 0.91$ cm.

Several experiments were performed to check the analytic models. The threshold energy requirement coupled with a large variation in the pulse voltage implies that the pulse length should be substantially narrower downstream (since all particles with insufficient energy are reflected). The 10-ns downstream pulse length was in rough agreement with predictions. The time evolution of beam width at various (z = constant) observation planes was studied with a streak camera. The maximum particle off-centering was shown to agree well with theory when the self-B_z field was negligible. Time-integrated measurements of beam thickness as a function of magnetic field imbalance also agree well. Finally, aperturing the beam to measure single particle coherent off-centering resulted in good agreement between experimental and analytical values for η and Δr_g.

2. Hot Cathode Experiments: The hot cathode device (Fig. 5) generates 26-kV, 1.0-A, 3-μs pulses, and the
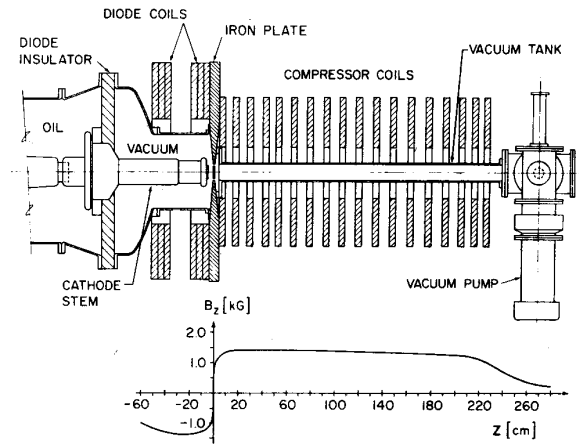

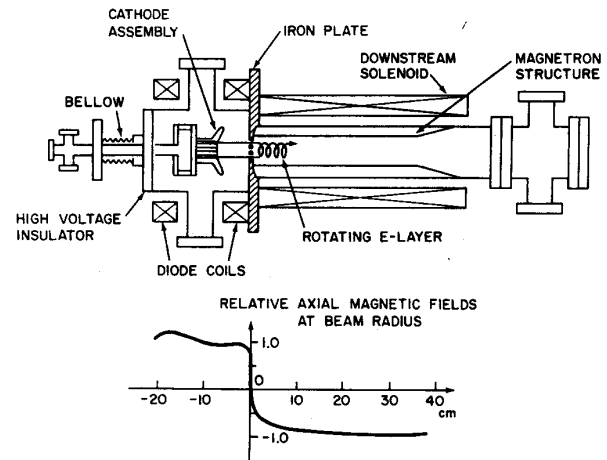Fig. 4. The cold cathode experimental configuration.

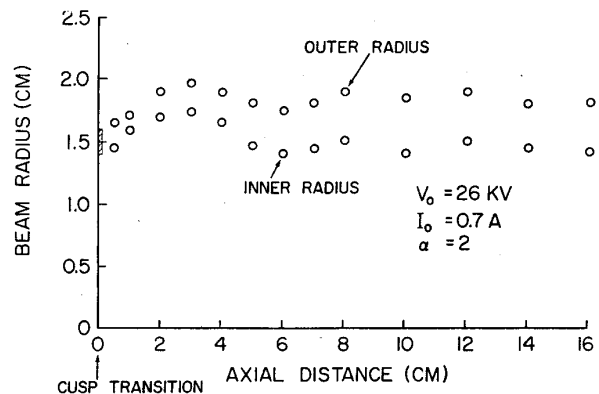Fig. 5. The hot cathode experimental configuration.

Fig. 6. Hot cathode beam envelope from fluorescent screen data.

beam is produced by a thermionic cathode with $r_0 = 1.5$ cm and $\Delta r = 0.2$ cm. The cusp is generated by pancake coils upstream and by a solenoid downstream, and the transition is shortened to $\zeta = 0.48$ cm by an iron plate. The evolution of beam thickness with axial location was measured with a movable fluorescent screen. Fig. 6 shows

a typical plot for a balanced cusp. The results agreed well with numeric simulations in both balanced and unbalanced operation. Estimates of Δr_g and λ also agreed fairly well with the analytic theory.

III. LARGE-ORBIT GYROTRON

The results of studies at the University of Maryland on cusp-injected large-orbit gyrotron (LOG) systems are presented in this section. Theoretical discussions appear in subsection A and two different sets of experimental studies are presented in subsection B.

A. Theoretical Discussion

In this subsection, the theoretical research performed in our group on the LOG system is summarized. The equilibrium state is described in Section III-A-1, the results of single particle motion in a single EM mode of a hollow cylindrical drift tube are detailed in Section III-A-2, and a self-consistent linear growth rate analysis for various wall configurations is presented in Section III-A-3. In Section III-A-4, brief comments on related issues are discussed.

1. The Equilibrium System: Particle Orbits–Wall Structures: We consider a rotating electron beam propagating in a cylindrical waveguide which is immersed in a uniform magnetic field $B_0\hat{z}$. The beam is assumed to be cold such that all electrons move on helical orbits centered about the system axis. The beam is assumed to have zero thickness with its equilibrium density given by

$$n_0(r) = n_s\delta(r - r_0) \qquad (7)$$

where r_0 is the equilibrium beam radius and n_s is the surface particle density. The beam is assumed to be tenuous so that the dc self-fields are neglected. Each electron has an initially unperturbed normalized velocity of $(0, \beta_{\theta_0}, \beta_{z_0})$, where $v_{\theta_0} = \beta_{\theta_0}c = r_0\Omega_0$.

The various cylindrical wall configurations considered are displayed in Fig. 7. In Fig. 7(a), the smooth wall configuration is shown. In addition to coaxial conductors of radii r_i, r_w, a dielectric liner along the outer wall with inner radius r_d is shown. The dielectric liner is considered as a means to "slow down" the velocity of EM waves so that they can resonantly interact with a low-energy rotating electron beam. In Fig. 7(b) and (c), the two periodic multiresonator magnetron-type wall structures that have been examined are shown. The first is called a vane resonator (VR) and the second a hole-and-slot resonator (HASR). The appropriate geometric quantities are indicated and labeled in the figures. The interface between the periodic structure and the interaction space that contains the rotating electron beam is at $r = r_w$ in both cases. We label this interface as the entrance to the "slots" for both geometries.

2. Single Particle Motion in Electromagnetic Fields [31]: The results of analytic and numeric studies of single particle motion in a given mode of the EM fields of a hollow cylindrical conductor are presented here. The model assumes that the E-layer is injected into a long drift
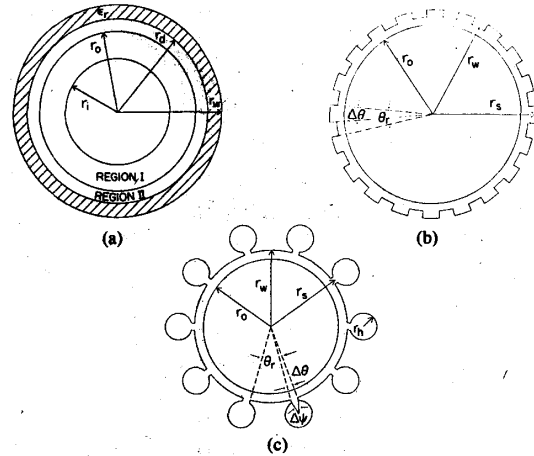

Fig. 7. Cross section of wall configurations: (a) coaxial system with a dielectric liner, (b) 20-slot VR, and (c) 10-slot HASR.

tube where a single empty waveguide TE mode is present with an azimuthal field component given by

$$E_\theta(r, \theta, z, t) = E_p J_l'(\alpha_{ln}r) \sin(\omega t - k_z z - l\theta) \qquad (8)$$

where J_l' represents the derivative of the ordinary Bessel function of order l, $\alpha_{ln} = p_{ln}'/r_w$, where p_{ln}' is the nth root of J_l', and k_z and ω are the wavenumber and frequency of the EM wave, respectively. For the empty waveguide mode, k_z and ω are related by the dispersion equation

$$\omega = c(k_z^2 + \alpha_{ln}^2)^{1/2}. \qquad (9)$$

Upon linearizing the relativistic single particle equations of motion and treating the EM field components as a linear term, a beam wave given by $\omega_B = l\Omega_0 + k_z v_{z_0}$ arises. Resonant interaction occurs at points in ω–k_z space where the beam line intersects the dispersion curve (i.e., $\omega_B = \omega$); this can happen only if

$$\frac{r_0}{r_w} \le \frac{l}{\alpha_{ln}r_w}\frac{\gamma_0\beta_{\theta_0}}{[1 + (\gamma_0\beta_{\theta_0})^2]^{1/2}}. \qquad (10)$$

There are generally two resonant intersections, denoted (ω_-^c, k_{z-}^c) and (ω_+^c, k_{z+}^c). The grazing condition occurs when $k_{z-} = k_{z+}$ and is generally the location of strongest EM–beam interaction.

The analysis is simplified if we transform to the beam frame. For resonant interactions near the grazing condition, the dominant force on the particle is due to the E_θ field. In Fig. 8, we display the beam frame particle trajectories with the cold cathode parameters chosen, with $l = 7$, $n = 1$, $r_w = 0.075$ m, $k_z = 27$ m^{-1}, and $E_p \simeq 10^6$ V/m. The cyclotron period is about 1.0 ns for these parameters. Specifically, we have plotted the azimuthal location of the particle in its cyclotron frame versus time. If the EM magnitude were zero, the particle trajectories would be straight horizontal lines. The dashed straight lines correspond to the azimuthal motion of the zeros of
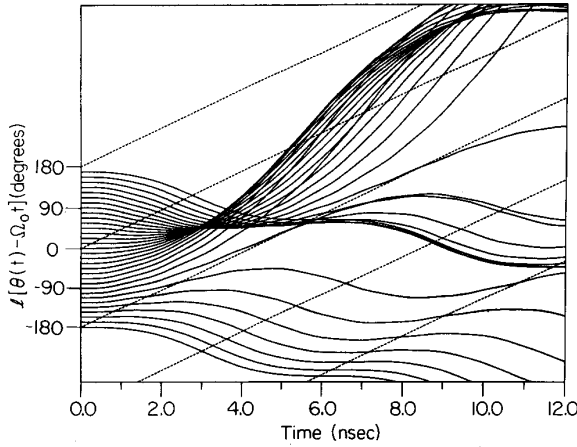
Fig. 8. Particle trajectories in one wave period. Cold cathode parameters with $l = 7$, $n_r = 1$, $k_z = 27$ m^{-1}, $E_p = 10^6$ V/m.

the E_θ field of the EM wave. The region between $-180°$ and $0°$ is the region of positive E_θ field. The following observations can be seen from Fig. 8. Bunching due to the negative mass effect ($d\gamma/dt$ term) is easily seen. This bunching is in phase (θ), but for a LOG produces strong spatial bunching as well. Trapping can also be seen as some particles do not cross the outer boundaries of the wave period, whereas some particles are untrapped and cross many wave periods. Another observation is that the particles bunch in the location of peak positive field for the example shown. If results for exact resonance were displayed, all particles would be trapped but the bunch would form in the region of zero field, resulting in no net energy transfer.

This simple analysis, though not self-consistent, demonstrates the trade-off between the percentage of trapped particles and the relative location of the bunch in the wave for net transfer of energy. In addition, this analysis indicates the dominant role that trapped particles play in energy transfer, being approximately an order of magnitude more important than untrapped particles. These expressions can be used to calculate the optimum frequency detuning from resonance for maximum energy transfer. For the parameters examined (which were optimized), about 55 percent of the particles are trapped, with the bunch forming near the peak positive E_θ field.

3. Self-Consistent Linear Growth Rate Analysis [10], [12], [13]-[16]:

In this section, we summarize a general self-consistent linear stability analysis of the interaction of a thin rotating beam in a cylindrical waveguide. Since the beam is thin (see (7)), a single particle analysis of the beam motion can be used in conjunction with Maxwell's equations. In Section III-A-3a, the analysis is described and a summary of results is given for the case of smooth wall geometries. In Section III-A-3b, the main result from which growth rates can be calculated for the periodic structures is presented.

  a. Smooth walls [13]: The linear growth rate problem is simplified in axisymmetric, large-orbit systems be-

cause perturbations with different harmonics do not interact. The Lorentz force equation is used to write the perturbed current in terms of the EM fields. When the synchronism condition is satisfied ($\psi_l \equiv \omega - \omega_B \ll \Omega_0$), the beam perturbations lie on the $r = r_0$ surface, and the equations are closed by calculating the discontinuity of the EM fields across the E-layer. The effects of the waveguide geometry are encapsulated into the geometry parameters:

$$g_{bb} = \frac{cB_z(r_0^+) - cB_z(r_0^-)}{r_0\partial_r cB_z\big|_{r_0}}\bigg|_{E_z(r_0)=0} \tag{11a}$$

$$g_{ee} = \frac{r_0\partial_r E_z\big|_{r_0^+} - r_0\partial_r E_z\big|_{r_0^-}}{E_z(r_0)}\bigg|_{\partial_r cB_z\big|_{r_0}=0} \tag{11b}$$

$$g_{be} = \frac{\partial_r E_z\big|_{r_0^+} - \partial_r E_z\big|_{r_0^-}}{i\partial_r cB_z\big|_{r_0}}\bigg|_{E_z(r_0)=0} \tag{11c}$$

and

$$g_{eb} = \frac{cB_z(r_0^+) - cB_z(r_0^-)}{iE_z(r_0)}\bigg|_{\partial_r cB_z\big|_{r_0}=0} \tag{11d}$$

The general dispersion relation is found from the analysis to be

$$\psi_l^2 (g_{bb}g_{ee} + g_{be}g_{eb}) = 2\left(\frac{\nu}{\gamma_0}\right)[g_{ee}\Omega_0^2 - (g_{be} + g_{eb})$$
$$\cdot \Omega_0\Omega_* - g_{bb}\Omega_*^2]. \tag{12}$$

The empty waveguide dispersion relation is obtained from (12) when $n_s = 0$:

$$D_e(\omega, k_z) = g_{bb}g_{ee} + g_{be}g_{eb} = 0 \tag{13}$$

and the general solution at resonance (13) is given by

$$\psi_l^3 = 2\left(\frac{\nu}{\gamma_0}\right)\frac{g_{ee}\Omega_0^2 - (g_{be} + g_{eb})\Omega_0\Omega_* - g_{bb}\Omega_*^2}{(g_{bb}g_{ee} + g_{be}g_{eb})'} \tag{14}$$

where $\nu = n_s e^2 r_0\mu_0/2m_0$ is Budker's parameter, $\Omega_* = k_z c - \omega\beta_{z0}$, and the prime denotes the derivative with respect to ω. We note that the frequency shift ψ_l depends only on ν/γ_0, the frequencies Ω_0 and Ω_*, and the geometry parameters. We write $\psi_l = \omega_r + i\Gamma$ so that $\Gamma > 0$ represents a growth in beam amplitude with time. Assuming the RHS of (14) to be real, the growth rate and frequency shift are given by

$$\Gamma = \frac{\sqrt{3}}{2}|\psi_l|^{1/3} \tag{15a}$$

$$\omega_r = \frac{-\text{sgn}(\psi_l^3)\Gamma}{\sqrt{3}} \tag{15b}$$

where sgn denotes the signum function.

For the case of only a smooth outer conductor, the hybrid parameters g_{be} and g_{eb} are zero and the dispersion

relation decomposes into TE modes defined by $g_{bb} = 0$ and TM modes defined by $g_{ee} = 0$. From (14) and (15), the growth rates at resonance are

$$\frac{\Gamma_{TE}}{\Omega_0} = \frac{\sqrt{3}}{2} \left[2 \frac{\nu}{\gamma_0} \frac{(c/r_w)^2}{\Omega_0 \omega} \right]^{1/3} \left| \frac{x_0 J_l'(x_0)}{[1 - (l/x_w)^2]^{1/2} J_l(x_w)} \right|^{2/3}$$

(16a)

and

$$\frac{\Gamma_{TM}}{\Omega_*} = \frac{\sqrt{3}}{2} \left[2 \frac{\nu}{\gamma_0} \frac{(c/r_w)^2}{\Omega_* \omega} \right]^{1/3} \left| \frac{J_l(x_0)}{J_l'(x_w)} \right|^{2/3}$$

(16b)

where $x(r) = r[(\omega/c)^2 - k_z^2]^{1/2}$, $J_l'(x_w) = 0$ for TE modes, and $J_l(x_w) = 0$ for TM modes. Two points deserve comment. First, these results (16) agree with the analysis of Sprangle in [6]. Second, grazing intersections are characterized by $\Omega_* = 0$, resulting in zero TM growth rates. In Fig. 9(a), the TE resonant growth rates as given by (16a) are plotted versus harmonic number l for the first radial mode. The parameters represent the cold cathode experiment. For these parameters, resonant interaction does not occur until the $l = 7$ harmonic. The TM modes do not have resonant interaction until the $l = 26$ harmonic (Fig. 9(b)), first radial mode, and so on for higher radial mode numbers. The figure indicates that the radiation spectrum will be rather broad-band, because the resonant growth rates decrease rather slowly with mode number.

The analysis leading to (12) is also valid in the synchronous nonresonant limit. However, nonresonant growth rates have $\Gamma \propto n_s^{1/2}$ whereas resonant growth rates have $\Gamma \propto n_s^{1/3}$, so that the latter dominate the former in the tenuous limit. In Fig. 10(a), the general growth rate is plotted versus k_z, with resonant points (from (16)) indicated by the squares. The corresponding beam line and the four lowest empty waveguide curves are plotted in Fig. 10(b). The interaction is strongest for the second TE radial mode, where the grazing condition is almost satisfied. The growth rates drop abruptly to zero at synchronous points below the empty waveguide curves. Above the dispersion curves, the growth rates drop off rapidly to small but finite values. In this example, interaction results in five frequency bands of instability.

When a dielectric liner is present, the empty waveguide cutoff frequencies are reduced, resulting in resonant interaction at lower harmonic numbers. In addition, the growth rates decrease substantially whenever the resonant intersection point occurs in ω-k_z space between the velocity of light line in free space and that in the dielectric. In this region, the field energy is mostly in the dielectric, with weak field amplitudes at the beam location. Calculations with the hot cathode parameters have indicated that growth rates drop off rapidly with harmonic, as expected.

b. *Periodic walls: VR and HASR [14], [16]:* For azimuthally periodic systems (with period $2\pi/n$), the general solutions can be written as a sum over the harmonic numbers l, which in general are all coupled to-
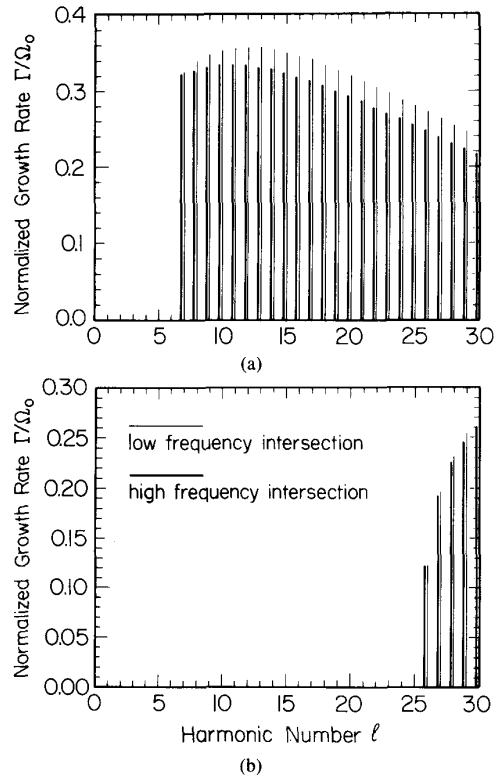

(a)

Harmonic Number ℓ

(b)

Fig. 9. Linear resonant growth rates versus harmonic number l for cold cathode parameters with hollow cylindrical wall structure: (a) TE mode and (b) TM mode. The thin line represents the low-frequency intersection, and the thick line represents the high-frequency intersection. Parameters: $n_s = 10^{14}$ m^{-2}, $\beta_{\theta_0} = 0.935$, $\beta_{z_0} = 0.305$, $r_0 = 0.06$ m, and $r_w = 0.075$ m.

gether. However, in the synchronous limit, the actual EM frequency is near one of the beam frequencies, say $l = l_0$. Then ψ_{l_0} is small, but $\psi_{l+n} \sim n\Omega_0$ is not small. Thus, the perturbed current contribution at $l = l_0$ dominates over all other l terms (because $J_l \propto \psi_l^{-2}$) and the smooth wall results are applicable. In addition, we restrict ourselves to only the fundamental mode interior to the periodic structure region. Since this implies that the fields across the slots are constant, we use an impedance matching technique for the boundary conditions at this interface. Also, in general, there can be a uniform phase shift between adjacent slots, provided that the total phase shift around the structure is a multiple of 2π.

VANE structure: Using the results presented in Section III-A-3a), the resonant growth rate is given by

$$\frac{\Gamma}{\Omega_0} = \frac{\sqrt{3}}{2} \left\{ \left(\frac{2\nu/\gamma_0}{x_w \Omega_0 \partial_\omega D(\xi)} \right) \left(\frac{\Delta\theta}{\theta_r} \right) \right.$$
$$\left. \cdot \left[\frac{\sin(l_0 \Delta\theta/2)}{l_0 \Delta\theta/2} \right]^2 \left[\frac{x_0 J_{l_0}'(x_0)}{J_{l_0}'(x_w)} \right]^2 \right\}^{1/3}$$

(17)

where the geometry is depicted in Fig. 7(b) and $1 \leq l_0 \leq n$. Recall that in leading up to this result, we must find the empty waveguide dispersion relation solution, given
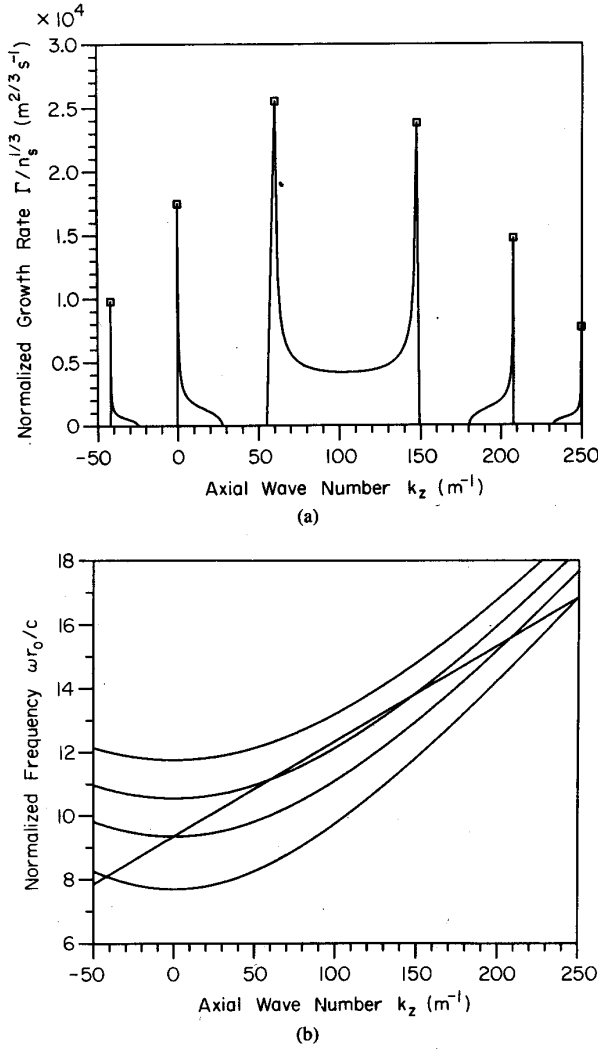
(a)

(b)

Fig. 10. The dependence of the growth rate on axial wavenumber: (a) growth rate along a beam line and (b) the corresponding dispersion curves. Parameters: $l = 11$, $n_r = 1$-3, $n_s = 10^8$ m^{-2}, $r_0 = 0.06$ m, $r_w = 0.10$ m, $\beta_{\theta_0} = 0.85$, and $\beta_{z_0} = 0.5$. Squares indicate single particle resonant growth rate results.

by

$$D(\xi) = D_s(\xi) - D_i(\xi) = 0 \qquad (18a)$$

where the slot term is

$$D_s = \frac{J_0(x_w) Y_0'(x_s) - Y_0(x_w) J_0'(x_s)}{J_0'(x_w) Y_0'(x_s) - Y_0'(x_w) J_0'(x_s)} \qquad (18b)$$

and the interaction region term is

$$D_i = \left(\frac{\Delta\theta}{\theta_r}\right) \sum_{q=-\infty}^{+\infty} \frac{J_{l_0+qn}(x_w)}{J_{l_0+qn}'(x_w)} \left\{\frac{\sin\left[(l_0 + qn)\Delta\theta/2\right]}{(l_0 + qn)\Delta\theta/2}\right\}^2. \qquad (18c)$$

Here $\xi = [(\omega/c)^2 - k_z^2]^{1/2}$. Because the dispersion relation depends only on ξ, the solutions are hyperbolas in the ω-k_z plane. Furthermore, the waveguide mode based

on harmonic l_0 has the same cutoff frequency as the mode based on harmonic $n - l_0$; thus, modes are labeled exclusively by their azimuthal content with acknowledgment of the above-mentioned degeneracy in the following manner: $(l_0, n - l_0)$. In this notation, the 2π mode would be labeled $(n, 0)$ and the π mode $(n/2, n/2)$. After finding the eigenfrequencies from (18a), the fields can be plotted. In Fig. 11, we have plotted the azimuthal electric field versus radius for a 2π mode. In Fig. 11(a), the $l = 0$ contribution is plotted, and in Fig. 11(b) the $l = n = 20$ contribution is shown. It is desirable to have the beam located at a maximum in the $l = 0$ term in addition to the strong direct coupling to the $l = 20$ term, which results in the unstable resonant interaction. As shown, this happens to be the case for the parameters chosen.

HASR structure: The procedure is similar to that above after making the additional assumption that the opening to the hole is small ($\Delta\psi \ll 2\pi$). The growth rate equation (17) is still valid provided we use

$$D(\xi) = D_h(\xi) + D_s(\xi) - D_i(\xi) \qquad (19a)$$

where

$$D_h^{-1}(\xi) = \left(\frac{\pi}{2}\right)^2 x_w x_s \left[J_0'(x_w) Y_0'(x_s) - Y_0'(x_w) J_0'(x_s)\right]$$

$$\cdot \left\{\left[J_0'(x_w) Y_0(x_s) - Y_0'(x_w) J_0(x_s)\right]\right.$$

$$+ \frac{\Delta\psi}{2\pi}\left[J_0'(x_w) Y_0'(x_s) - Y_0'(x_w) J_0'(x_s)\right]$$

$$\left.\cdot \sum_{m=-\infty}^{+\infty} \frac{J_m(x_h)}{J_m'(x_h)}\left[\frac{\sin(m\Delta\psi/2)}{m\Delta\psi/2}\right]^2\right\}. \qquad (19b)$$

Again, through proper selection of geometry parameters, strong coupling can be realized with modes dominated by the holes. Analytic results are shown and compared with experimental results in the next section.

4. Discussion of Related Issues: There are three issues that deserve comments. The first is related to the finite radial thickness of the E-layer. A fluid analysis for finite thickness E-layers was presented in [32], where it was concluded that thick, tenuous beams in resonant systems must be operated near cutoff, $k_z \approx 0$. The rapid decrease in growth rate as the axial wavelength decreases is attributed to the loss of synchronism with a large fraction of the E-layer particles because of the spread in canonical angular momentum resulting from cusp injection.

The second issue is related to the low-energy LOG device, where we find that linear growth rates are extremely small. That is, in one pass through the RF structure, the beam electrons give up only a small portion of their energy. However, the beam pulse is relatively long ($\gtrsim 1$ μs) for the low-energy device and thus the EM fields build up gradually with time. There have been many calculations [18], [34], [35] related to start-up conditions in such de-
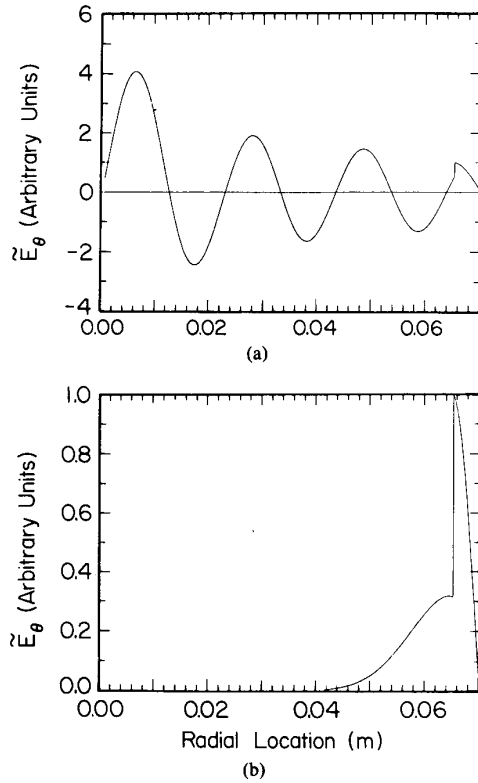
Fig. 11. The VR empty waveguide E_θ field at the center of the slot opening: (a) the $l = 0$ component and (b) the $l = n$ component. The 20-slot VR parameters: $n = 20$, $n_r = 7$, $r_w = 0.0652$, $r_s = 0.070$ m, and $\Delta\theta/\theta_r = 0.535$.

vices, and they appear to have more relevance than linear growth rates.

The third issue is related to overall system design considerations and related nonlinear effects. The procedures relative to gyrotron devices were presented in [26] and [33], the former giving a very detailed analysis for a LOG amplifier.

B. Experimental Discussion

1. Cold Cathode Experiments [9]-[12], [14], [15]: Early experiments were performed on a high-voltage pulse line accelerator (2-3-MeV, 20-30-kA, 30-ns FWHM), in a configuration shown schematically in Fig. 4. Two solenoids are used to form the magnetic cusp, and the downstream solenoid is extended to provide a drift region in which the electron motion is essentially adiabatic. A hollow, nonrotating electron beam of radius 6 cm is field emitted from a carbon knife-edge cathode located 7.5 cm from a planar anode mounted on the iron plate. The electrons pass through an annular slit on the anode, and the effective area of the slit may be varied to provide some control over the amount of current that passes through the cusp into the downstream region. In addition, all electrons below the threshold energy for transmission through the cusp transition are reflected, and the resultant downstream current pulse is considerably shorter in duration

than the diode current waveform. The observed microwave pulse duration is comparable to the downstream current pulse duration. Typical downstream beam parameters are 2-3 MeV, 1-8 kA, and 5-15 ns.

Microwave radiation was extracted axially from the device by way of a transitioning horn antenna and a large-diameter vacuum window. A fraction of the output power was then picked up by an open-ended waveguide and dispersed through 40 m of waveguide to determine the frequency spectra of the microwave pulses. Total microwave power inferred from these measurements was confirmed in several cases by microwave calorimetry.

Table I lists relevant experimental parameters for three different experimental configurations investigated using this facility. In the first case, the rotating electron beam interacts with a simple cylindrical conducting boundary, and radiation is produced by resonant interaction between beam cyclotron modes and the TE and TM modes of the cylindrical waveguide. The experimental results for this configuration are shown in Fig. 12, and indicate that in the absence of any mode control mechanism, the observed radiation is broad-band, as expected from the theoretical results. Although the integrated power over all frequencies can be high (1-100 MW) in this configuration, the peak power at any one frequency is fairly low (10-400 kW), and overall electronic efficiency is only 1-2 percent.

In the second case, the rotating beam interacts with the modes of a 20-slot multiresonator vane-type magnetron circuit, shown in Fig. 7(b), designed to operate in the 2π mode at approximately the 20th cyclotron harmonic, about 16 GHz. Results of both theory and experiment for this case are shown in Fig. 13 and indicate the dramatic improvement in mode control, peak power, and overall electronic efficiency (about 10 percent) that the resonant structure provides.

The third case studied is microwave production from rotating beams interacting with a 10-slot HASR, shown in Fig. 7(c). Results of both theory and experiment for this configuration are shown in Fig. 14 and indicate that the HASR system can perform at a level comparable to the vane resonator system described previously.

Recently, a similar experimental configuration was constructed at Los Alamos National Laboratory. This ex-
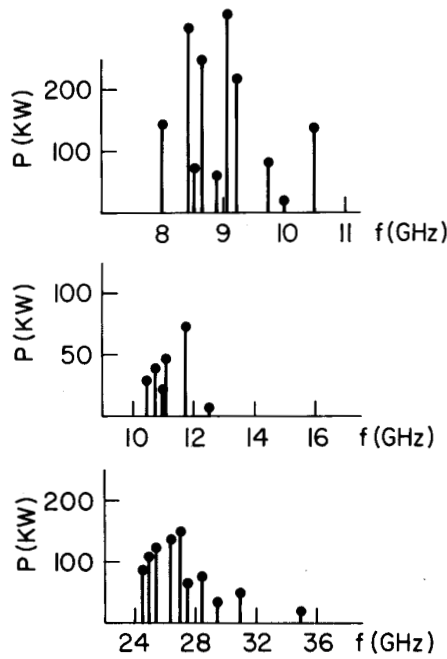
TABLE I
COLD CATHODE LOG PARAMETERS

	Smooth Wall	Vane Resonator	Hole and Slot
Electron Energy (MeV)	2.2	2.2	2.2
Beam Radius (cm)	6	6	6
Axial Magnetic Field (gauss)	1,400	1,450	1,300
$\alpha = B_\theta/B_z$	3	3.8	1.75
Cyclotron Frequency (MHz)	739	765	686
r_w (cm)	7.5	6.5	6.8
r_s (cm)	N/A	7.0	7.0
r_h (cm)	N/A	N/A	1.2
N (No. of slots)	N/A	20	10
$\Delta\theta/\theta_r$	N/A	0.535	0.147

Fig. 12. Radiated power from LOG with smooth 7.5-cm radius cylindrical conducting boundary. Data cover X band, Ku band, and Ka band.
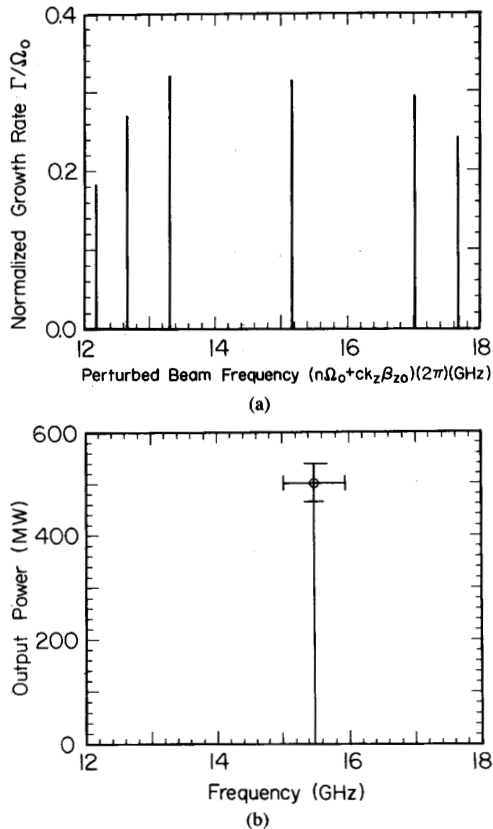

Fig. 13. (a) Linear growth rates for 20-slot VR system. Beam parameters: $n_s = 10^{14}$ m^{-2}, $\beta_{\theta_0} = 0.951$, $\beta_{z_0} = 0.250$, $r_0 = 0.06$ m. The growth rate at 15.2 GHz is for the grazing condition with the $n = 7$ radial mode. (b) Radiated microwave spectrum from the 20-slot VR system. Diode magnetic field 1450 G, downstream field 1500 G.
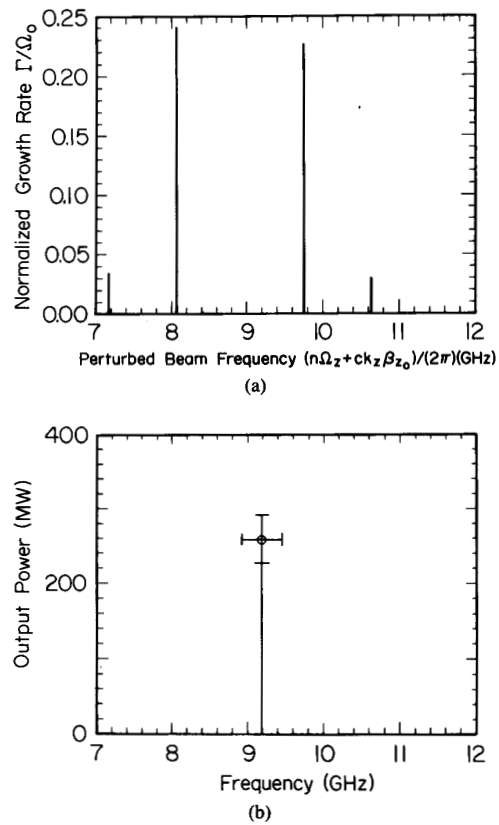

Fig. 14. (a) Linear growth rates for ten-slot HASR system. Beam parameters: $n_s = 10^{14}$ m^{-2}, $\beta_{\theta_0} = 0.854$, $\beta_{z_0} = 0.487$, $r_0 = 0.06$ m. The growth rates for 7.2 and 10.6 GHz are for the $n = 4$ radial mode, and those at 8.1 and 9.7 GHz are for the $n = 5$ radial mode. (b) Radiated power spectrum from the ten-slot HASR system. Magnetic field 1300 G.

periment is designed to operate at about 600 kV, 1–10 kA, 70 ns FWHM, and is unique in that the field coils were placed within the vacuum envelope, resulting in a very compact device. Initial experiments, summarized in Table II, were designed to operate at the third cyclotron harmonic (2 GHz) using a three-slot vane resonator. The theoretically predicted growth rate for the device in this configuration is shown in Fig. 15. As waveguide at this frequency to efficiently extract the radiation was not immediately available, the radiation field was sampled by a small-diameter (1 cm) magnetic $\dot{B}$ probe and fed directly to a Tektronix 7104 oscilloscope for frequency determination. A typical waveform is shown in Fig. 15, and indicates that operation has been achieved at the predicted frequency of 2 GHz. Although the device is currently being operated unloaded, the amplitude of the radiation field sampled by the small magnetic probe is consistent with total microwave power at this frequency of 10–50 MW, implying an electronic efficiency of several percent. Experiments to more carefully determine the actual extractable power from the device are currently in progress.

2. Hot Cathode Experiments [16], [36]: A similar configuration was constructed to investigate microwave production at more modest electron energies and currents

TABLE II
LOS ALAMOS LOG PARAMETERS

Electron Energy (keV)	600
Beam Radius (cm)	6.52
Axial Magnetic Field (gauss)	478
$\alpha = \beta_\theta/\beta_z$	3
Cyclotron Frequency (MHz)	615
r_w (cm)	7.63
r_s (cm)	9.3
N (No. of slots)	3
$\Delta\theta/\theta_r$	0.5

TABLE III
HOT CATHODE LOG PARAMETERS

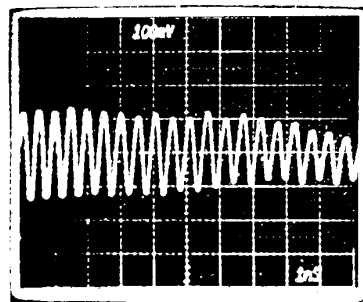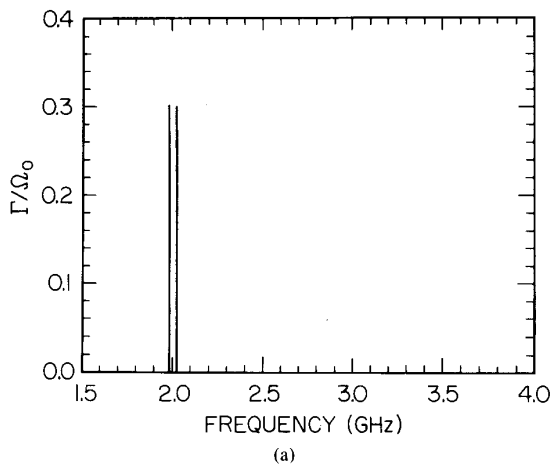|	
Electron Energy (keV)	26
Beam Radius (cm)	1.5
Axial Magnetic Field (gauss)	312
$\alpha = \beta_\theta/\beta_z$	2
Cyclotron Frequency (MHz)	875
r_w (cm)	1.8
r_s (cm)	2.19
N (No. of slots)	10
$\Delta\theta/\theta_r$	0.5

(a)

(b)

Fig. 15. (a) Linear growth rates for the three-slot Los Alamos VR system. Beam parameters: $n_x = 1.7 \times 10$, $\beta_{\theta_0} = 0.842$, $\beta_{z_0} = 0.281$, $r_0 = 0.0652$ m. The two growth rates are for near grazing intersection with the 2π mode for $n = 1$. (b) Microwave waveform indicating 2-GHz operation from a $\dot{B}$ probe output fed directly into a Tektronix 7104 oscilloscope.

using conventional thermionic cathode technology. This experiment, shown schematically in Fig. 5, was designed and constructed by Namkung [36], who first reported successful operation employing a six-slot vane resonator system. Recent experiments on this device by Chojnacki *et al.* [16] have confirmed the potential of the configuration to produce high harmonic wave generation at relatively high electronic efficiency levels. The basic experimental parameters are summarized in Table III.

In the experiments, a mildly relativistic rotating electron beam (25–30-kV, 1–2-A, 5-μs FWHM) interacts with the modes of a ten-slot vane resonator designed to operate in the 2π mode at 8.9 GHz. Radiation in these experiments was extracted axially as in the cold cathode experiments, and the extraction efficiency was measured by careful cold-cavity excitation of each mode by a low-power sweep oscillator. The 60-Hz repetition rate and longer pulse duration of the experiment allowed use of a spectrum analyzer for frequency determination. Results of theoretical calculations, shown in Fig. 16(c), indicate that operation should be possible in the (8, 2) and (9, 1) modes as well. In fact, growth rates for the (8, 2) mode are somewhat higher than those for the 2π mode.

Experimental results, shown in Fig. 16(a) and (b) for both the 2π and (8, 2) modes, respectively, indicate that narrow-band (5-MHz line width) operation of the device has been achieved in both modes by careful variaton of experimental parameters. Operation in both modes simultaneously has not been observed at any significant power levels. The estimated efficiency of operation in the 2π mode at the tenth harmonic is approximately 14 percent $\pm$ 8 percent. The estimated efficiency of operation in the (8, 2) mode at or near the eighth harmonic is approximately 42 percent $\pm$ 24 percent. The large errors in the measured efficiencies are associated with possible errors in the measurement of the microwave extraction efficiency. This latter figure is surprisingly high, and not fully understood theoretically at the present time.

IV. CIRCULAR GEOMETRY FREE-ELECTRON LASERS

Investigation of circular geometry free-electron lasers has been conducted in collaboration with researchers at M.I.T. [37]–[40]. The configuration studied is a refinement of the rippled field magnetron, first proposed by Bekefi [41]. In these experiments, the rotating electron beam interacts with an essentially transverse wiggler magnetic field produced by samarium–cobalt magnets interior and/or exterior to the beam, as shown in Fig. 17. The magnets are placed behind metal cylinders in such a way that the beam sees only smooth conducting boundaries. Radiation is then coupled out of the system via one of the TM waveguide modes of the coaxial or cylindrical conducting boundary system.
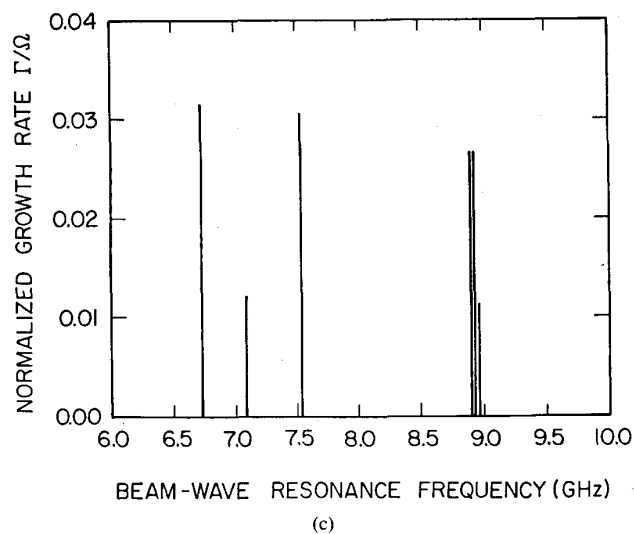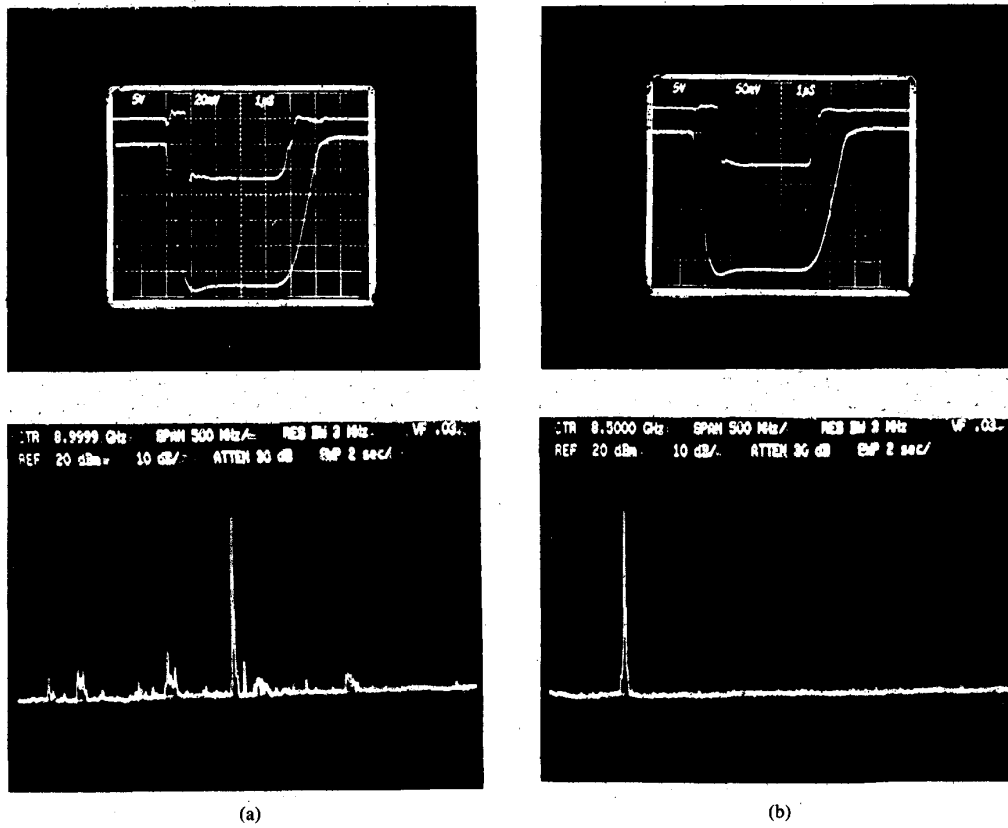
(a)   (b)

BEAM-WAVE RESONANCE FREQUENCY (GHz)

(c)

Fig. 16. (a) Detector response (top), diode voltage pulse (middle, 5 kV/division), and spectrum analyzer trace (bottom) for 2π mode excitation. Instantaneous microwave power 2.2 ± 1.32 kW at 8.85 GHz with efficiency 14 percent $\pm$ 8 percent at 28 keV and 0.56 A. (b) As in (a) but for (8, 2) mode excitation. Instantaneous microwave power 9.1 ± 5.2 kW at 6.78 GHz with efficiency 42 percent $\pm$ 24 percent at 27 keV and 0.8 A. (c) Linear growth rates for the ten-slot, hot cathode VR system. Growth rates at 8.91 GHz are for the 2π mode, at 6.73 and 7.53 GHz for the (8, 2) mode, and at 7.08 and 8.96 GHz for the (9, 1) mode (not observed).
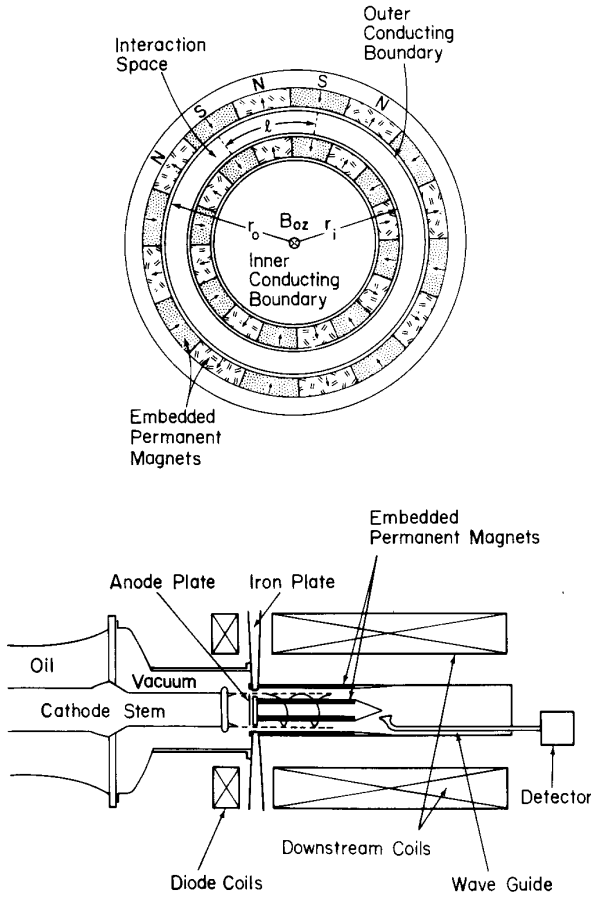
Fig. 17. Schematic of circular geometry FEL experiment.

A. Theoretical Discussion

Beyond the cusp, the beam electrons move in the presence of the combined axial and wiggler magnetic fields, which can be approximated (subject to the condition that $\nabla \cdot \vec{B} = \nabla \times \vec{B} = 0$ in the region between two conducting boundaries of radius r_0 and r_i) by the expression

$$\vec{B} = \hat{r} \frac{B_{0_w}}{2} \left[\left(\frac{r}{r_0} \right)^{N-1} + \left(\frac{r_i}{r} \right)^{N+1} \right]$$

$$\cdot \left(\frac{r_0}{r_i} \right)^{(N^2-1)/2N} \exp \left[iN\theta \right]$$

$$+ \hat{\theta}i \frac{B_{0_w}}{2} \left[\left(\frac{r}{r_0} \right)^{N-1} - \left(\frac{r_i}{r} \right)^{N+1} \right]$$

$$\cdot \left(\frac{r_0}{r_i} \right)^{(N^2-1)/2N} \exp \left[iN\theta \right] + \hat{z}B_z. \quad (20)$$

Here, $\hat{r}$, $\hat{\theta}$, and $\hat{z}$ are unit vectors in the radial, azimuthal, and axial directions, respectively, $N = \pi(r_0 + r_i)/l$ is the number of spatial periods around the azimuth, l_0 is the linear periodicity specified midway in the gap, and B_{0_w} is the amplitude of the radial component of the field at a distance $r = (r_0^{N-1} r_i^{N+1})^{1/2N}$, where the azimuthal com-

ponent vanishes. In this case, the field is primarily radial near the center of the gap and the undulatory force is mostly in the z direction.

If only the outer magnets are present, the field may be approximated by the expression

$$\vec{B} = \left\{ B_{0_w} \left(\frac{r}{r_0} \right)^{N-1} \exp \left[iN\theta \right] \right\}$$

$$\cdot (\hat{r} + \hat{\theta}i) + \hat{z}B_z. \quad (21)$$

Single particle motion in the presence of these fields has been studied numerically, and typical results are shown in Fig. 18. For the case where the beam electrons rotate in the presence of both inner and outer magnets, the undulation is primarily axial, as expected, and the orbits are almost unperturbed in the x-y plane. In the case where the inner magnets are removed, a significant precession in the electron orbits is predicted in a direction counter to the electron motion. Thus, the actual effective beam cyclotron frequency must be reduced by the precession frequency in this case to accurately describe the beam cyclotron modes.

In either case, the radiative process has been identified as the coupling of a "synchronous mode," upshifted in frequency by the wiggler periodicity N,

$$\omega = (l + N)\Omega_0 + k_z v_z \quad (22)$$

to one or more of the TM waves supported by the coaxial conducting boundary system. If v_θ and k_θ are identically zero (the case where electron propagation and wave propagation are both purely circular), the radiation frequency is given by

$$\omega = \frac{N\Omega_0}{1 - [l\Omega_0/\omega_c(l, m)]} = \frac{k_\omega v_\theta}{1 - (v_\theta/v_{p\theta})}. \quad (23)$$

Here $k_\omega = 2\pi/l_0$ and $\omega_c(l, m)$ is the cutoff frequency for the TM$_{lm}$ mode, where l and m are the azimuthal and radial wavenumbers, respectively, and

$$v_{p\theta} = \omega_c(l, m) \left(\frac{r}{l} \right) \quad (24)$$

is the phase velocity in the azimuthal direction of the RF perturbation. It is interesting to compare this result to the dispersion relation for a conventional linear free-electron laser:

$$\omega = \frac{k_\omega v_0}{1 - (v_0/c)} \quad (25)$$

where v_0 is the axial electron velocity.

In the case where v_z and k_z are nonzero (as in the experiments), the radiation growth occurs near the crossing points of the beam mode and the waveguide mode given by

$$\omega^2 = k_z^2 c^2 + \omega_c^2(l, m). \quad (26)$$

Maximum growth rate is expected to occur at the tangential intersection of these two waves. At this point the ra-
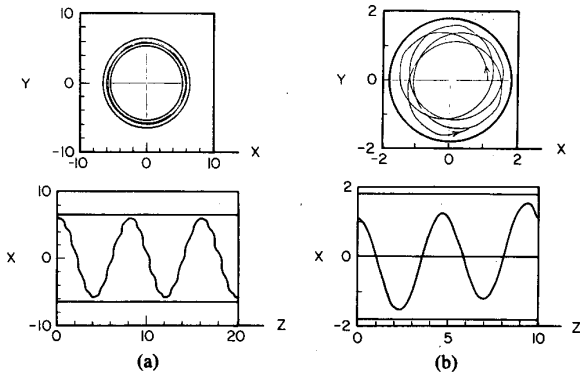
Fig. 18. Computer-generated electron orbits in the x-y and x-z planes for (a) electrons injected at $r = 0.06$ m and $\beta_{\theta_0} = 0.96$, $\beta_{z_0} = 0.20$ into combined axial and wiggler magnetic fields with $B_z = 1400$ G, $B_{0_w} = 1300$ G ($n = 6$, both interior and exterior magnets), and (b) electrons injected at $r = 0.014$ m and $\beta_{\theta_0} = 0.269$, $\beta_{z_0} = 0.148$ into combined axial and wiggler magnetic fields with $B_z = 345$ G and $B_{0_w}/r_0^{N-1} = 7.153 \times 10^{14}$ T/m^9 ($N = 10$, exterior magnets only).
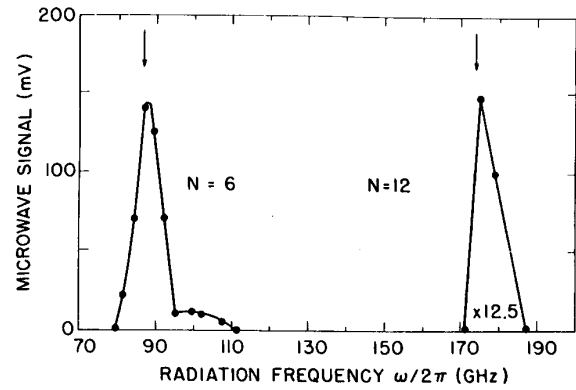

Fig. 19. Measured microwave spectra for cold cathode circular FEL experiments operated with six and 12 wiggler periods around the azimuth ($r_0 - r_i = 0.011$ m).

TABLE IV
COLD CATHODE CIRCULAR GEOMETRY PARAMETERS

	N = 6	N = 12
Electron Energy (MeV)	2.2	2.2
Beam Radius (cm)	6	6
Axial Magnetic Field (gauss)	1,400	1,400
$\alpha = \beta_\theta/\beta_z$	3	3
Cyclotron Frequency (MHz)	739	739
r_0 (cm)	6.51	6.51
r_i (cm)	5.39	5.39
ℓ_0 (cm)	6.28	3.14
Wiggler Field Amplitude (gauss)	1,300	1,300

diation frequency is given by

$$\omega = \gamma_z \omega_c(l, m) = \gamma_z^2(l + N)\Omega_0 \qquad (27)$$

where $\gamma_z = [1 - (v_z/c)^2]^{-1/2}$.

Schuetz et al. [42] have reported that the interaction can also occur when the synchronous mode is down-shifted by the number of wiggler periods:

$$\omega = (l - N)\Omega_0 + v_z k_z. \qquad (28)$$

Recently, Saito and Wurtele [43] have reported a theoretical analysis of this configuration that indicates that because the rotating electron beam is subject to the negative mass instability, circular geometry FEL's of this type can be expected to have greater gain and efficiency than comparable linear FEL's. They do appear to be even more susceptible to a degradation in performance due to energy spread in the injected beam electrons than are linear devices, however.

B. Experimental Discussion

1. Cold Cathode Experiments: Table IV summarizes the parameters used for the initial high-power cold cathode experiments. Radiation has been observed at both 90 GHz ($N = 6$) and 180 GHz ($N = 12$) at peak power levels in the range 10–20 MW, corresponding to an electronic efficiency of about 1 percent. Typical radiation spectra obtained with a grating spectrometer for frequencies above 74 GHz are shown in Fig. 19 for $N = 6$ and $N = 12$. Although the measured radiation frequencies are in reasonable agreement with theoretical predictions, the theory also predicts enhanced emission at low frequencies (about 27 GHz for the $N = 6$ case). Experiments are currently under way to determine if the lower frequency emission can be observed as well.

In an attempt to determine to what extent the close proximity of the coaxial conducting boundaries is inhibiting the negative mass instability, an experiment is cur-

rently in progress in which the gap between the coaxial conductors has been increased from 11 mm to 17 mm. This results, however, in an accompanying loss of wiggler field strength, reducing the amplitude of the radial component of the field to about 600 G at the center of the gap. A preliminary radiation spectrum obtained for this case ($N = 6$) is shown in Fig. 20, and indicates that the emission is decidedly less narrow-band than in the previous work. Theoretical and experimental investigations of this phenomenon are currently in progress.

2. Hot Cathode Experiments: For these experiments, the device constructed for the low-energy large-orbit gyrotron studies was modified to replace the multiresonator magnetron circuit with a smooth cylindrical outer conducting boundary housing ten periods of samarium–cobalt magnets around the azimuth. As design considerations prohibited the use of an inner magnet array, the field in the interaction region has components both transverse and parallel to the rotation of the beam electrons. In addition, the absence of the inner magnets results in a significant precession in the electron orbits, as discussed previously.

Table V summarizes the parameters used in the hot cathode studies of this configuration. The experiment was originally designed to operate at the up-shifted cyclotron
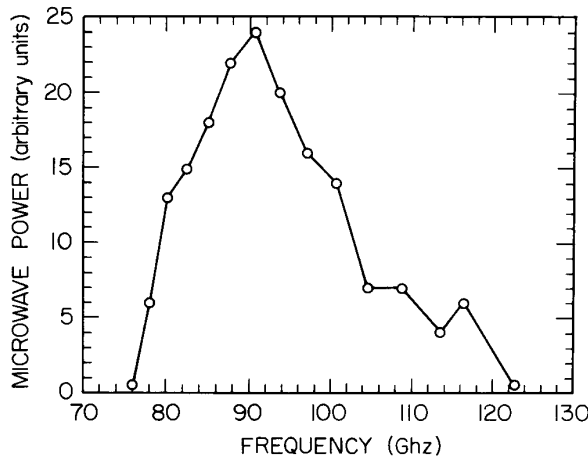
Fig. 20. Measured microwave spectra for cold cathode circular FEL experiment operated with six wiggler periods around the azimuth ($r_0 - r_i = 0.017$ m).

TABLE V
HOT CATHODE CIRCULAR GEOMETRY PARAMETERS

Electron Energy (keV)	27
Beam Radius (cm)	1.5
Axial Magnetic Field (gauss)	448
$\alpha = \beta_\theta/\beta_z$	2.23
Cyclotron Frequency (MHz)	1,127
r_0 (cm)	1.8
ℓ_0 (cm)	0.942
N (No. of periods)	10
Wiggler Field Amplitude (gauss)	270

harmonic ($l + N = 11$) in the TM_{11} mode. Because of the unexpected precession in the electron orbits, interaction at the up-shifted cyclotron harmonic was not possible since the beam mode, now represented by

$$\omega = (l + N)(\Omega_0 - \omega_{pr}) + k_z v_z$$

did not intersect the waveguide mode. As a result, the experimental fields were adjusted to allow for operation at the down-shifted ($N - l = 9$) harmonic.

Typical results from the experiment, shown in Fig. 21, indicate that narrow-band radiation with a linewidth of about 50 MHz has been produced at the down-shifted ($N - l = 9$) cyclotron harmonic at 10.15 GHz. Unfortunately, to bring the ninth harmonic beam line into tangential intersection with the TM_{11} mode line, asymmetric cusp operation was required and the downstream beam quality was severely degraded. Total observed microwave power was about 100 W, corresponding to an electronic efficiency of about 1 percent.

These results should allow the design of a next-generation experiment designed to operate more efficiently at the up-shifted cyclotron harmonic, and such studies are currently under way.

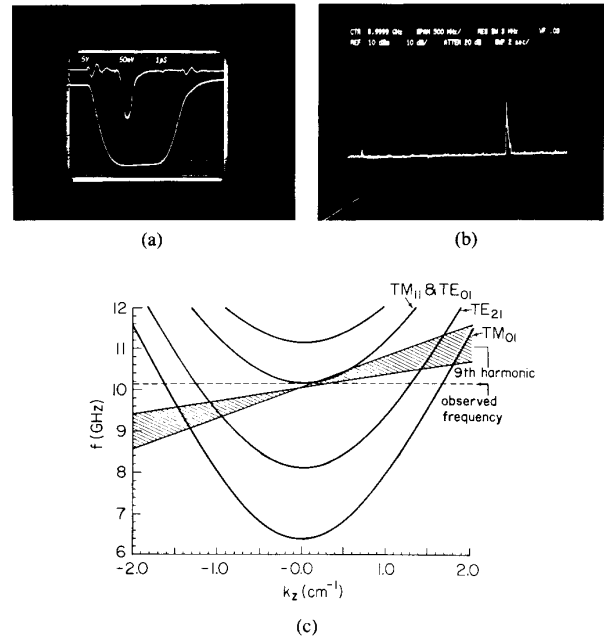(a)   (b)

(c)

Fig. 21. Hot cathode circular FEL experimental results. (a) Microwave signal (top) and diode voltage waveform (bottom, 5 kV/division). (b) Spectrum analyzer trace for TM_{11} excitation, ~100 W at 10.15 GHz with efficiency ~1 percent at 26 keV, 0.4 A. (c) Intersection in phase space of ninth harmonic precession-corrected beam line with the TM_{11} mode.

V. ENERGY RECOVERY FROM SPENT BEAM

A. Conceptual Basis

Large-orbit devices can operate in a high-harmonic mode with a correspondingly reduced magnetic field. However, efficiency in high-harmonic operation is usually lower than for small-orbit gyrotrons operating in the fundamental mode. Consequently, a substantial fraction of the original beam energy remains in the spent beam.

The overall efficiency of the device can be considerably enhanced by using energy recovery techniques. The overall device efficiency η_T is related to the intrinsic efficiency η and the efficiency of energy recovery η_R by the relationship

$$\eta_T = \frac{\eta}{1 - \eta_R(1 - \eta)}. \tag{29}$$

Thus, a device with an intrinsic efficiency of 10 percent, if augmented by an energy recovery system of 75-percent efficiency, can give an overall efficiency of 31 percent.

A technique for energy recovery which is well established in linear beam tubes is based on the use of depressed collectors [44]. However, these alone will not suffice in the case of spiraling electron beams. For energy recovery, the electrons have to do work against an electrostatic field. Thus, conversion of the rotational motion of the electrons into axial streaming motion becomes necessary before the beam proceeds on to depressed collectors.
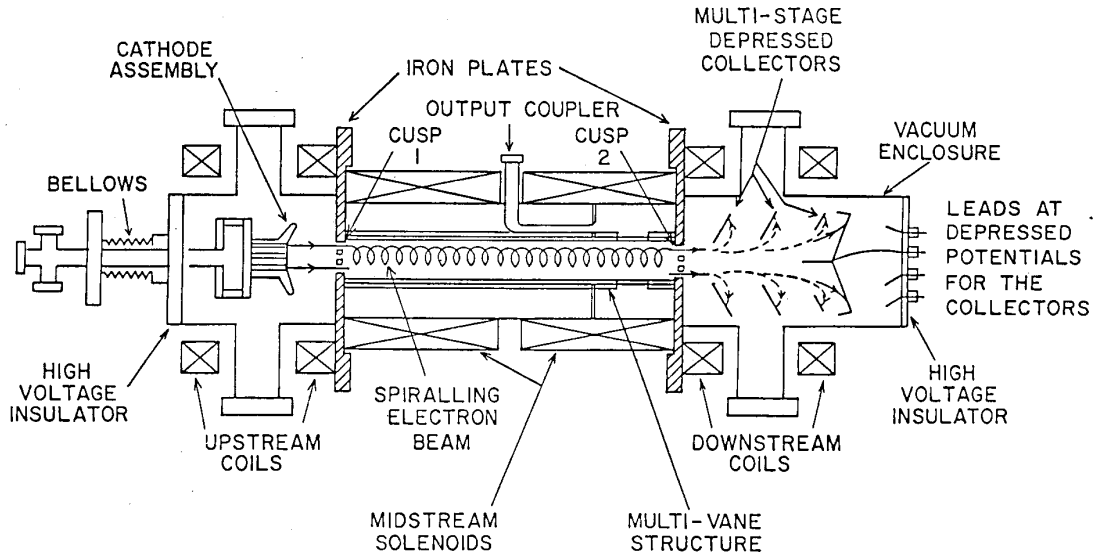
Fig. 22. Schematic diagram of a proposed experimental setup for energy recovery. A Pierce gun generates an axially streaming hollow beam. The first cusp converts it into a spiraling beam for RF interaction, and the second cusp unwinds it for delivering a large fraction of residual energy to depressed collectors.

We have proposed the use of a second magnetic cusp in a large-orbit gyrotron to perform this beam conditioning function. A schematic diagram of the arrangement is shown in Fig. 22. A hollow beam of electrons is generated by a Pierce-type gun with an annular cathode immersed in a field $-B_0\hat{z}_0$. The first magnetic cusp encountered by the beam turns it into an axis-encircling beam. The second cusp returns the magnetic field to $-B_0\hat{z}$ and largely transforms the rotational motion of the spent beam into axial motion. The radial magnetic field component interacts with the azimuthal velocity to generate the required axial component of force.

B. Simulation of Unwinding of the Beam

A parameter that provides an index of the rotational versus axial motion of the beam is α, defined as

$$\alpha \triangleq \frac{v_\perp}{v_\parallel}. \tag{30}$$

The changes in its value as the beam passes through the first cusp ($\alpha_{midrange}$) and then the second cusp ($\alpha_{residual}$) have been studied [45] using a single particle trajectory code. Variations in relevant input parameters relating to the cusp widths, their mutual separation, the magnetic field, the accelerating voltage V_0, and the starting radius of the particle r_0 were simulated one at a time using the hot cathode LOG experimental values [16]. The magnetic field in the cusps is modeled by (6). Typical values are V_0 = 26 kV, B_0 = 328.8 G, r_0 = 1.5 cm, and ζ = 4 mm, and the distance between the two cusps is 30 cm.

The results indicate that the average value of $\alpha_{residual}$ is lower than $\alpha_{midrange}$ by a factor of more than 10 in typical cases, as is shown in Figs. 23 and 24. For low-energy
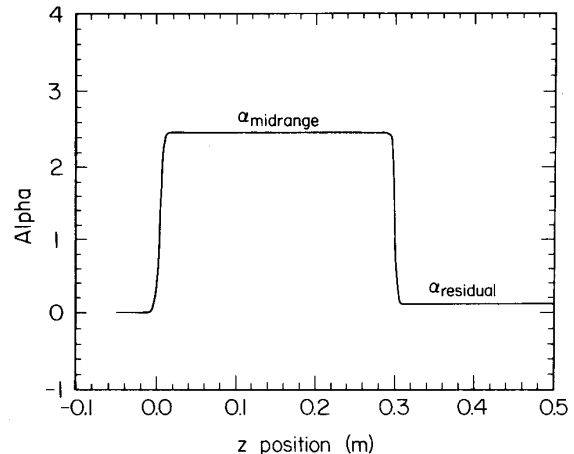

Fig. 23. Simulation of the effect of two cusps on alpha defined as $v_\perp/v_\parallel$. As the electrons pass the first cusp at 0 cm, α rises from zero to $\alpha_{midrange}$. When the electrons cross the second cusp at 30 cm, α falls again to a low value $\alpha_{residual}$.

beams, kinetic energy varies as the square of the velocity, indicating that the energy of rotational motion in the beam after passage through the second cusp would be less than 1 percent of the energy in axial motion. The finite cusp widths result in finite values of $\alpha_{residual}$, which in turn results in finite guiding center radii and scalloping motion.

Simulations indicate that the $\alpha_{residual}$ varies cyclically with starting radius, magnetic field, and distance between cusps. In each case, the parameter affects the scalloping wavelength and the phase of scalloping in which the particle enters the second cusp. The $\alpha_{residual}$ goes through minima when the scalloping motion of the electrons is inwards at the entrance to the second cusp.
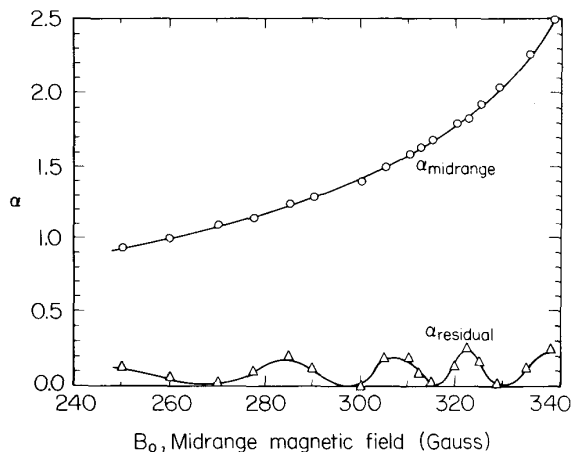
Fig. 24. Simulation of variation of $\alpha_{midrange}$ and $\alpha_{residual}$ with B_0, the magnitude of the magnetic field. $\alpha_{midrange}$ rises monotonically with B_0. $\alpha_{residual}$ goes through cyclic changes, but is considerably smaller than $\alpha_{midrange}$.
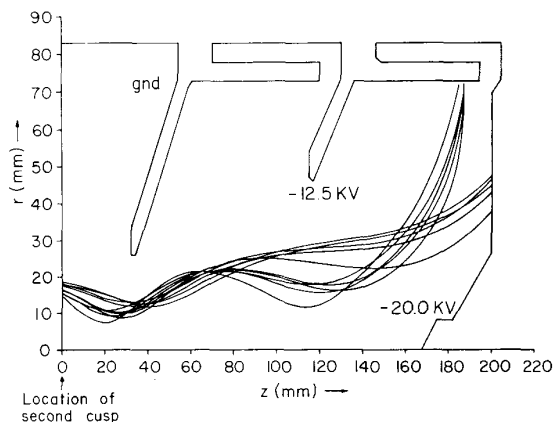

Fig. 25. An illustration of energy sorting in the region of depressed collectors. Beamlets emerge from the second cusp at angles simulated by single particle code. Beamlets of energies 26 keV and 20.8 keV are collected on electrodes at −20 kV and −12.5 kV, respectively.

Another conclusion from these studies is that the $\alpha_{residual}$ varies slowly with the width of the second cusp. This cusp can have a width two or three times that of the first cusp. This in turn makes it possible to have a larger gap for the spent beam to pass through. It thus takes into account a likely increase in beam thickness.

C. Energy Sorting and Depressed Collectors

In order to obtain a large collector efficiency, it is common practice to use a number of depressed electrodes. This number corresponds to the number of groups into which the electrons in the beam are sorted. The objective is to keep the difference between the energy of the electrons and the potential on the depressed collector to the minimum feasible for each group.

In the present case, the energy sorting is done by the combined action of a magnetic field and an electrostatic field. The starting point for the simulation of trajectories was the output from the single particle code. The values of ζ for the first and second cusps were taken to be 4 mm and 10 mm, respectively. The Herrmannsfeldt code [28] was used to trace the trajectories in the collector region.

Various geometries and potentials of the electrodes as well as different magnetic field profiles are being examined in the simulation of trajectories in the collector region. Fig. 25 shows one particular case in which there are three collectors at zero, −12.5 kV, and −20 kV, respectively. Two beamlets are shown, which enter the collector region at energies of 26 keV and 20.8 keV. In both cases, the location and angles of trajectories at the output of the second cusp are those given by the single particle code. In the latter case, a decrease in energy of 20 percent has been introduced at the midpoint between the cusps as a first-order method of simulating energy loss to RF by some beamlets. It is seen that the two beamlets are collected at the electrodes at −20 kV and −12.5 kV, respectively, demonstrating energy sorting. Other beamlets were given

an energy change of −30 percent, −10 percent, and +10 percent. They were collected at the electrodes at −12.5 kV, −20 kV, and −20 kV, respectively. When the electronic efficiency of the device is of the order of 15 percent, the spread in energies would be adequately covered in this way. If the electronic efficiency is higher, a larger number of depressed collectors would be appropriate.

In this way, the principles of unwinding the electron beam by a second cusp, and that of energy sorting in the collector region, have been verified by simulations. Recovery efficiencies of at least 75 percent appear feasible as a result of these studies. Steps are being taken toward an experimental verification.

VI. CONCLUSIONS

Large-orbit microwave devices are now well enough understood to allow for a tentative assessment of their capabilities relative to other available microwave devices. For example, LOG oscillators have operated at very high harmonics (6–20) of the electron cyclotron frequency at electronic efficiencies in excess of 20 percent. These devices have been operated in both highly relativistic and mildly relativistic regimes, at microwave output powers as high as 600 MW at the 20th harmonic. While not as efficient as small-orbit gyrotron oscillators operating at the fundamental of the cyclotron frequency, the ability of LOG devices to operate single mode at high harmonic frequencies with reasonable efficiency is presently unmatched. In addition, studies that we have conducted indicate that energy recovery from the spent electrons appears to be somewhat more straightforward for large-orbit devices than for small-orbit gyrotrons (although energy recovery in linear devices is considerably easier than for either gyrotron configuration).

To date, however, less work has been reported on LOG amplifiers [22], [26]. In addition, although it should be a straightforward matter, little work has been reported on microwave power extraction directly from the resonators.

This approach to power extraction in a vane-resonator device would result in direct RF extraction in the more desirable rectangular TE_{10} mode.

Circular geometry FEL's, on the other hand, are at a much less advanced state of development. Although the concept should allow for the construction of an FEL oscillator without external mirrors because of the feedback provided by the recirculation of the wave in the device, applicable theory and simulation has only recently been available and initial experiments have not been designed for optimum operation. An assessment of the attractiveness of this new class of FEL's for specific applications will have to await the results of new experiments more carefully designed for operation in a selected parameter range.

REFERENCES

[1] A. Faltens, G. R. Lambertson, J. M. Peterson, and J. B. Rechen, "Observations on collective longitudinal instabilities in electron rings," in *Proc. IXth Int. Conf. High Energy Accelerators* (Stanford, CA), 1974, pp. 226-229.

[2] V. P. Sarantsev, "Collective linear acceleration of ions," in *Proc. VIIIth Int. Conf. High Energy Accelerators* (CERN, Geneva), 1971, pp. 289-294.

[3] U. Schumacher, C. Andelfinger, and M. Ulrich, "Collective acceleration of protons and helium ions in the Garching ERA," *IEEE Trans. Nucl. Sci.*, vol. NS-22, pp. 989-991, 1975.

[4] W. W. Destler, D. W. Hudgings, R. A. Kehs, P. K. Misra, and M. J. Rhee, "Single particle and collective effects observed in the electron beam of the Maryland ERA experiment," *IEEE Trans. Nucl. Sci.*, vol. NS-22, pp. 995-998, 1975.

[5] H. Jory, "Investigation of electronic interaction with optical resonators for microwave generation and amplification," Final Report, Contract ECOM-01873-F, Varian Associates, July 1968 (unpublished).

[6] V. L. Granatstein, R. K. Parker, and P. Sprangle, "Cyclotron resonance phenomena in microwave and submillimeter radiation from an intense electron beam," in *Proc. Int. Topical Conf. Electron Beam Res. Technol.* (Albuquerque, NM), 1975, vol. II, pp. 401-423.

[7] P. Sprangle, "Excitation of electromagnetic waves from a rotating annular relativistic E-beam," *J. Appl. Phys.*, vol. 47, no. 7, pp. 2935-2940, 1976.

[8] H. S. Uhm and R. C. Davidson, "Kinetic description of negative-mass instability in an intense relativistic nonneutral E-layer," *Phys. Fluids*, vol. 20, pp. 771-784, 1977.

[9] W. W. Destler, D. W. Hudgings, M. J. Rhee, S. Kawasaki, and V. L. Granatstein, "Experimental study of microwave generation and suppression in a non-neutral E layer," *J. Appl. Phys.*, vol. 48, pp. 3291-3296, 1977.

[10] W. W. Destler, H. Romero, C. D. Striffler, R. L. Weiler, and W. Namkung, "Intense microwave generation from a non-neutral rotating E-layer," *J. Appl. Phys.*, vol. 52, no. 4, pp. 2740-2749, 1981.

[11] W. W. Destler, R. L. Weiler, and C. D. Striffler, "High-power microwave generation from a rotating E-layer in a magnetron-type waveguide," *Appl. Phys. Lett.*, vol. 38, no. 7, pp. 570-572, 1981.

[12] W. W. Destler, R. Kulkarni, C. D. Striffler, and R. L. Weiler, "Mi-

crowave generation from rotating electron beams in magnetron-type waveguides," *J. Appl. Phys.*, vol. 54, no. 7, pp. 4152-4162, 1983.

[13] W. Lawson and C. D. Striffler, "A general linear growth rate formula for large orbit, annular electron beams," *Phys. Fluids*, vol. 28, no. 9, pp. 2868-2877, 1985.

[14] W. Lawson, W. W. Destler, and C. D. Striffler, "High power microwave generation from a large orbit gyrotron," *IEEE Trans. Plasma Sci.*, vol. PS-13, p. 444, 1985.

[15] W. Lawson, W. W. Destler, and C. D. Striffler, "High power microwave radiation from a large orbit gyrotron," *IEEE Trans. Nucl. Sci.*, vol. NS-32, pp. 2960-2962, 1985.

[16] E. Chojnacki, W. W. Destler, W. Lawson, and W. Namkung, "Studies of microwave radiation from a low-energy rotating electron beam in a multiresonator magnetron cavity," *J. Appl. Phys.*, vol. 61, pp. 1268-1274, 1987.

[17] Y. Y. Lau and L. R. Barnett, "Theory of a low magnetic field gyrotron (gyromagnetron)," *Int. J. Infrared Millimeter Waves*, vol. 3, no. 5, pp. 619-644, 1982.

[18] K. R. Chu and D. Dialetis, "Theory of harmonic gyrotron oscillator with slotted resonant structure," *Int. J. Infrared Millimeter Waves*, vol. 5, no. 1, pp. 37-56, 1984.

[19] W. Namkung and J. Y. Choe, "Experimental results of cusptron microwave tube study," *IEEE Trans. Nucl. Sci.*, vol. NS-32, pp. 2885-2887, 1985.

[20] H. S. Uhm, C. M. Kim, and W. Namkung, "Linear theory of cusptron microwave tubes," *Phys. Fluids*, vol. 27, pp. 488-498, 1984.

[21] D. B. McDermott, N. C. Luhmann, Jr., D. S. Furuno, A. Kupiszewski, and H. R. Jory, "Operation of a millimeter-wave harmonic gyrotron," *Int. J. Infrared Millimeter Waves*, vol. 4, no. 4, pp. 639-664, 1983.

[22] K. R. Chu, D. S. Furuno, N. C. Luhmann, Jr., D. B. McDermott, P. Vitello, and K. Ko, "Theory, design, and operation of large orbit high harmonic gyroklystron amplifiers," *IEEE Trans. Plasma Sci.*, vol. PS-13, pp. 435-443, 1985.

[23] L. R. Barnett, J. M. Baird, P. S. Rha, U. A. Shrivastava, and R. W. Grow, "Millimeter wave gyrotron/peniotron experiments," in *Proc. 1985 IEEE Int. Conf. Plasma Sci.* (Pittsburgh, PA), June 3-5, 1985, pp. 6-7.

[24] M. J. Rhee and W. W. Destler, "Relativistic electron dynamics in a cusped magnetic field," *Phys. Fluids*, vol. 17, pp. 1574-1581, 1974.

[25] W. W. Destler and M. J. Rhee, "Radial and axial compression of a hollow electron beam using an asymmetric magnetic cusp," *Phys. Fluids*, vol. 20, pp. 1582-1584, 1977.

[26] W. Lawson and P. E. Latham, "The design of a small-orbit/large-orbit gyroklystron experiment," *J. Appl. Phys.*, vol. 61, pp. 519-528, 1987.

[27] W. Lawson, "Design of low velocity-spread cusp guns for axis encircling beams," *Appl. Phys. Lett.*, vol. 50, pp. 1477-1479, 1987.

[28] W. B. Herrmannsfeldt, SLAC Report No. 226, Nov. 1979.

[29] W. W. Destler, P. K. Misra, and M. J. Rhee, "Relativistic electron dynamics in a cusped magnetic field with a downstream drift region," *Phys. Fluids*, vol. 18, pp. 1820-1822, 1976.

[30] W. Namkung, W. Lawson, and D. Byun, "Microwave generation from a cusptron device," *Bull. Amer. Phys. Soc.*, vol. 28, p. 1060, 1983.

[31] H. Bluem, P. E. Latham, W. Lawson, and C. D. Striffler, "Single particle motion in a large orbit gyrotron," *IEEE Trans. Microwave Theory Tech.*, vol. MTT-35, pp. 946-955, Nov. 1987.

[32] W. Lawson and C. D. Striffler, "A linear growth rate fluid formulation for large orbit, annular electron layers with finite thickness," *Phys. Fluids*, vol. 29, no. 5, pp. 1682-1694, 1986.

[33] K. R. Chu, V. L. Granatstein, P. E. Latham, W. Lawson, and C. D. Striffler, "A 30 MW gyroklystron-amplifier design for high-energy linear accelerators," *IEEE Trans. Plasma Sci.*, vol. PS-13, no. 6, pp. 424-434, 1985.

[34] P. Vitello, W. H. Miner, and A. T. Drobot, "Theory and numerical modeling of a compact low-field high-frequency gyrotron," *IEEE Trans. Microwave Theory Tech.*, vol. MTT-32, pp. 373-386, 1984.

[35] P. Vitello, "Cyclotron maser and peniotron-like instabilities in a whispering gallery mode gyrotron," *IEEE Trans. Microwave Theory Tech.*, vol. MTT-32, pp. 917-921, 1984.

[36] W. Namkung, "Observation of microwave radiation from a cusptron device," *Phys. Fluids*, vol. 27, pp. 329-330, 1984.

[37] G. Bekefi, R. E. Shefer, and W. W. Destler, "Millimeter wave emission from a rotating electron ring in a rippled magnetic field," *Appl. Phys. Lett.*, vol. 44, pp. 280-282, 1984.

[38] W. W. Destler, F. M. Aghamir, D. A. Boyd, G. Bekefi, R. E. Shefer,

and Y. Z. Yin, "Experimental study of millimeter wave radiation from a rotating electron beam in a rippled magnetic field," *Phys. Fluids*, vol. 28, pp. 1962-1967, 1985.

[39] G. Bekefi, R. E. Shefer, and W. W. Destler, "Millimeter wave radiation from a rotating electron ring subjected to an azimuthally periodic wiggler magnetic field," *Nucl. Instrum. Methods*, vol. 250, pp. 352-356, 1986.

[40] E. Chojnacki and W. W. Destler, "Microwave radiation from a low-energy rotating electron beam in an azimuthally periodic magnetic field," *IEEE J. Quantum Electron.*, vol. QE-23, pp. 1605-1609, 1987.

[41] G. Bekefi, "Rippled-field magnetron," *Appl. Phys. Lett.*, vol. 40, pp. 578-580, 1982.

[42] L. S. Schuetz, E. Ott, and T. M. Antonsen, Jr., "Analysis of a wideband, rotating-beam free-electron laser," *Phys. Fluids* (to be published).

[43] H. Saito and J. Wurtele, "Comparison between circular and conventional free electron lasers," in *Proc. 10th Int. Conf. Infrared Millimeter Waves* (Lake Buena Vista, FL), 1985, pp. 43-44.

[44] H. G. Kosmahl, "Modern multistage depressed collectors, A review," *Proc. IEEE*, vol. 70, pp. 1324-1334, 1982.

[45] A. Singh, E. Chojnacki, W. W. Destler, D. Goutos, V. L. Granatstein, W. Lawson, and C. D. Striffler, "Efficiency enhancement by using depressed collector techniques for devices employing gyrating electron beams," in *Proc. IEEE Int. Conf. Plasma Sci.*, June 1987, p. 40.